



City Research Online

City, University of London Institutional Repository

Citation: Justino Vaz, M. G., Karathanassis, I. K., Gavaises, M. & Mouokue, G. (2025). Influence of needle-geometry design on in-nozzle flow characteristics for fuel flexibility on marine engines. *International Journal of Engine Research*, 14680874251398815. doi: 10.1177/14680874251398815

This is the published version of the paper.

This version of the publication may differ from the final published version.

Permanent repository link: <https://openaccess.city.ac.uk/id/eprint/36479/>

Link to published version: <https://doi.org/10.1177/14680874251398815>

Copyright: City Research Online aims to make research outputs of City, University of London available to a wider audience. Copyright and Moral Rights remain with the author(s) and/or copyright holders. URLs from City Research Online may be freely distributed and linked to.

Reuse: Copies of full items can be used for personal research or study, educational, or not-for-profit purposes without prior permission or charge. Provided that the authors, title and full bibliographic details are credited, a hyperlink and/or URL is given for the original metadata page and the content is not changed in any way.

City Research Online:

<http://openaccess.city.ac.uk/>

publications@city.ac.uk



Influence of needle-geometry design on in-nozzle flow characteristics for fuel flexibility on marine engines

Marilia G. Justino Vaz¹ , Ioannis K. Karathanassis¹,
Manolis Gavaies¹ and Gerard Moukue²

Abstract

The design and positioning of the needle are crucial factors that determine the morphology and dynamics of the flow within the nozzle flow of modern fuel injectors. Their optimization is crucial for enhancing the quality of the air-fuel mixture and ensuring compliance with stringent international emission regulations for marine powertrains. This study compares three needle-tip geometries with a reference design utilized in marine injectors. Numerical simulations were employed to analyze the flow characteristics induced by these needle geometries at two needle-lift positions. These correspond to two operational modes typically employed to ensure fuel flexibility: low-lift for dual-fuel mode and high-lift for Diesel-only mode. A multiphase model coupled with thermodynamic closure derived via the Perturbed Chain Statistical Associating Fluid Theory (PC-SAFT) Equation of State (EoS) was utilized. In order to minimize the computational cost associated with this EoS, the thermodynamic and transport properties of the fuel were computed beforehand and saved in a structured table. The results demonstrated strong predictive capability with computational costs typically accepted for industrial design time scales. In low-lift positions, the flow was attached to the inner surfaces, due to the high velocity imposed by the narrow flow area of the needle seat. The base needle design exacerbates cavitation, but two of the proposed designs significantly reduce the cavitation intensity. This led to a significant decrease in the amount of fuel vapor forming inside the injector compared to the base design. Furthermore, one design relocates most of the cavitation area beyond the spray hole. At higher-lift positions, the designs can be categorized into two groups regarding the overall flow structure. The first one exhibits flow patterns similar to the base design and the second one exhibits reduced nozzle flow coefficients.

Keywords

dual-fuel, fuel flexibility, pilot injection, PC-SAFT, needle design, marine injector, in-nozzle flow

Received: 23 March 2025; accepted: 28 October 2025

Introduction

Global warming is now widely acknowledged as a major issue with potentially devastating consequences. The transportation sector contributes significantly to greenhouse gas emissions owing to the usage of fossil fuels. As a consequence, strict emissions regulations like EURO VI in Europe and Tier IV in the US have been implemented.^{1,2} In order to be compliant with such mandates, there is a strong focus on either hybridization or fully electrifying passenger cars and, to some extent, heavy-duty vehicles. However, electrification is currently not a viable option for marine transport and heavy-duty Diesel applications which is the reason that Internal Combustion Engine (ICE) remains the foreseen energy converter in these applications.³

Currently, maritime vessels predominantly operate with Diesel fuel, while dual-fuel mode with a gas fuel as primary fuel is also utilized.⁴ This latter allows, under certain conditions, a smooth transition between the two modes while the engine is running.⁵ This versatility

¹City St George's, University of London, London, UK

²Woodward L'Orange GmbH, Stuttgart, Germany

Corresponding authors:

Marilia G. Justino Vaz, City St George's, University of London, School of Science & Technology, Northampton Square, London EC1V 0HB, UK.
Email: Marilia.Justino-Vaz@citystgeorges.ac.uk

Ioannis K. Karathanassis, City St George's, University of London, School of Science & Technology, Northampton Square, London EC1V 0HB, UK.
Email: Ioannis.Karathanassis@citystgeorges.ac.uk

provides safe operation during dual-fuel operation, even if issues such as abnormal combustion arise. Furthermore, it facilitates compliance with emission regulations in air-quality controlled areas and fuel selection according to cost and availability.^{6,7}

However, this fully flexible configuration imposes constraints related to the injection system complexity.⁸ Specifically, it requires the use of multiple Diesel injectors, with at least one being located in a decentralized manner in the combustion chamber,⁹ or an injector with a complex geometric design featuring multiple nozzles or needles. The optimal solution would be a single Diesel direct injector that efficiently delivers fuel for the entire range of engine operations. This includes delivering small quantities for dual-fuel mode and larger quantities for Diesel-only mode.

This single Diesel injector architecture presents technical challenges due to the significant differences in injection and flow characteristics between the two modes.¹⁰ The injector must guarantee precise spray targeting and penetration for both modes, each of which has distinct requirements for ignition and flame propagation. In order to accomplish fine atomization and proper mixing with the gas fuel, dual-fuel operation often necessitates higher injection pressures in comparison to the Diesel-only mode. Nevertheless, the same injector needs to handle the pressure requirements of Diesel-only mode while maintaining optimal performance. This dual operation requirement poses challenges in terms of injector design and durability. Although it is possible to utilize the same Diesel injector for both modes, it is still necessary to carefully evaluate and optimize the injector performance and flow capacity for each mode.

In the last three decades, extensive research has been carried out to elucidate in-nozzle flow during fuel injection. Experiments, facilitated by developments in high-speed imaging, can provide a representative visualization of the two-phase flow field within transparent nozzle replicas using optical, X-ray, and, more recently, neutron measurements.^{11–13} Nonetheless, such measurements are quite challenging in real injector geometries operating at high pressure/temperature conditions.

Computational Fluid Dynamics (CFD) simulations can provide complementary information under realistic operating conditions. Cavitation models suited for fuel injectors,^{14,15} as well as modeling closures for high-order thermodynamics and fuel properties transport^{16,17} are widely used. Besides, the high injection pressure necessary to meet emission legislation imposes significant variations in the fuel properties.^{18,19} Steep pressure gradients, particularly at low needle lifts, lead to cavitation manifested as string (vortex) and geometry-induced cavitation.²⁰

Cavitation in fuel injectors can have negative or positive effects on injector performance. It may contribute to cycle-to-cycle variations in fuel delivery²¹ and enhance spray cone angle, velocity coefficient and atomization.^{22,23} Nonetheless, its collapse near solid

surfaces can inflict damage on the injector walls, lead to erosion, and in severe situations, cause deterioration in injector performance and eventual injector failure.²⁴

In particular, the needle-tip directly influences the flow structure in the sac volume, especially for low needle lifts. It also contributes to the effective volume of the sac, which plays a role in vortex formation, cavitation, and unsteady flow.^{14,25} A larger sac tends to generate a more stable flow with less turbulence as pressure fluctuations are dampened.²⁶ However, the larger sac volume might lead to the remaining fuel slowly dripping out into the combustion chamber after an injection event and contribute to an increase of hydrocarbon emissions.²⁷

On the other hand, a smaller sac volume creates a more confined flow path, accelerating the fuel through a restricted passage, which might lead to more localized and intense cavitation near the needle seat.²⁶ The increased turbulence and cavitation can lead to a more dispersed spray with a wider cone angle and finer atomization. It also makes the design susceptible to flow fluctuations, manufacturing tolerances, and needle misalignment.²⁸

Salvador et al.²⁹ compared a micro-sac and a Valve-Covered Orifice (VCO) Diesel injector, where the micro-sac nozzles demonstrated a superior discharge coefficient and effective injection velocity relative to VCO nozzles. The existence of a small volume upstream of the discharge orifices in micro-sac nozzles influences the formation and intensity of cavitation. Watanabe et al.³⁰ compared the recirculation zones of three needle-tip designs with different seat angles and resulting in different sac volumes in a mini-sac nozzle. They observed that the geometry of the needle-tip affects the vortex flow in the nozzle sac. The needle with a larger angle increased vortical cavitation, but the vortex flow in the sac may be reduced at lower angles. A reduced needle-tip angle results in increased spray penetration and a constant injection rate, accompanied by a smaller spray cone angle. Markov et al.³¹ examined the influence of grooves on the needle-tip, which imposed localized hydraulic resistance in a VCO nozzle. This resistance amplified flow turbulence, increased the turbulent kinetic energy at the orifice outlet and induced cavitation within the nozzle. As a result, the fuel atomization was improved. However, it adversely affected the mass flow rate and flow velocity.

Although the previous investigations underscore the importance of nozzle geometrical parameters in the performance of Diesel injectors. Nearly all investigations focused on the nozzle geometry,^{29,32–35} with only a reduced number concentrating specifically on the needle-tip geometry, and even less focused on their influence on marine applications. Due to the market dominance, most of the research topics have historically focused on light-duty applications over marine injectors.³⁶ Besides, the needle-tip redesign is often simpler to implement, requiring less extensive re-tooling or manufacturing changes and is cost-effective compared

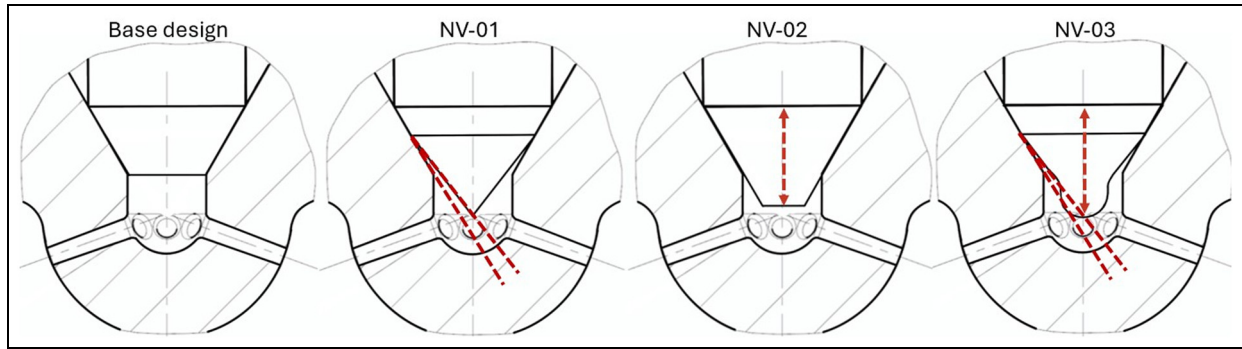


Figure 1. Comparative view of the base design and the three proposed needle-tip modifications.

to the injector modifications. Hence, the aim of the current work is to investigate the influence of needle-tip design on the in-nozzle flow and cavitation for marine injectors. Furthermore, this study proposes an improved design suitable for fuel flexibility throughout the entire engine operation range. This type of injector is typically used for small-to medium-sized marine engines, with an average displacement volume of 5 L per cylinder. For that, the potential of needle-tip geometrical modifications is investigated through CFD calculations, where three needle-tip designs were proposed and compared to a base design. Moreover, dual-fuel and Diesel-only operation modes were emulated using a fixed set of needle lifts (54 and 480 μm) to isolate the geometrical influence on the in-flow conditions. However, it should be noted that this does not capture the full range of dynamic behavior during real engine operation.

Following this short introduction, the paper is divided into five sections. The second section gives an outline of the proposed needle-tip designs. The third section describes the numerical method, case set-up and validation of the enhanced CFD model by the inclusion of NIST and PC-SAFT EoS fluid properties calculations in a thermodynamic closure. Then, the effects of the needle-tip on cavitation and flow characteristics for two operation modes are analyzed in the fourth section. Finally, the conclusion is presented in the fifth section, where one of the proposed designs presents a better trade-off for the studied marine injector.

Needle-tip geometries

The needle-tip geometries simulated correspond to a marine Diesel injector design provided by Woodward L'Orange (WLO). The modification of the needle-tip directly impacts the sac volume. The base design is a Diesel injector with 7 straight holes (K-factor equal to 0) with a spray hole diameter greater than 300 μm . For reasons of confidentiality, the specific geometrical values cannot be disclosed. Figure 1 shows the base design as well as the three proposed modifications, where the geometry of the nozzle and needle seat remain identical in all variations.

In the first needle-tip variation, NV-01, a deflection angle was incorporated on the first third of the needle-tip through a minor elevation. This angle creates a diverging section between the needle-tip and needle seat, increasing the cross-section downstream of the throat. In addition, the needle-tip was extended into a conical form, thereby reducing sac volume variation. After these alterations, the sac volume is reduced by 7.5% compared to the base design.

The second variation, NV-02, focuses on the impact of a reduced sac volume. Therefore, the shape and angles of the base design were kept constant. To achieve a volume decrease, the needle form was elongated along the vertical axis, resulting in a 21.5% reduction. Finally, the third variation, NV-03, integrates the primary features of the two previously described designs: divergent section, volume reduction, and needle-tip elongation. The deflection angle remained constant in the initial third of the needle-tip, resulting in a significant volume reduction of 27.5% due to the needle's elongation into a spherical form. In addition, rounding was included in the transition areas to avoid sharp corners.

Simulation framework

Numerical method

A numerical approach for the in-nozzle two-phase flow is applied; the three working media present in a fuel injection process include the liquid fuel, fuel vapor, and ambient gas (nitrogen). Fuel and ambient gas are modeled as homogeneous mixtures in mechanical and thermal equilibrium.³⁷ In addition, a diffuse interface approximation is assumed at the liquid-gas interface. A pressure-based flow solver is employed using the finite volume method. The numerical framework comprises the governing equations described below, along with the thermodynamic closure.

- Mixture mass conservation

$$\frac{\partial \rho}{\partial t} + \nabla \cdot (\rho \vec{v}) = 0 \quad (1)$$

where ρ is the mixture density and \vec{v} is the velocity vector field.

- Mixture momentum equation

$$\frac{\partial(\rho\vec{v})}{\partial t} + \nabla \cdot (\rho\vec{v}\vec{v}) = -\nabla p + \nabla \cdot (\vec{\tau}) \quad (2)$$

where p is the static pressure and $\vec{\tau}$ is the stress tensor representing the moment transfer due to all the turbulent fluctuations for Reynolds-Averaged Navier-Stokes (RANS) equations.

- Species transport equation

$$\frac{\partial \rho_l y_{fuel}}{\partial t} + \nabla \cdot (\rho_l \vec{v} y_{fuel}) = -\nabla \cdot \vec{J} \quad (3)$$

where y_{fuel} the fuel mass fraction and \vec{J} the mass diffusion flux.

- Mixture energy equation

$$\frac{\partial \rho E}{\partial t} + \nabla \cdot [v(\rho E + p)] = \nabla \cdot ((k_{eff} \nabla T) + (h\vec{J}) + (\vec{\tau} \cdot \vec{v})) \quad (4)$$

where T is the temperature and h is the specific enthalpy as a function of pressure and temperature.

RANS and Unsteady Reynolds-Averaged Navier-Stokes (URANS) can predict cavitation in high-pressure operating conditions.^{24,38} The turbulence closure employed here is the Shear-Stress Transport (SST) $k-\omega$ model. In addition, a correction is applied to turbulent viscosity to account for the two-phase mixture compressibility effects,³⁹ as shown in equation (5).

$$\mu_t = f(\rho) \frac{a_1 k}{\max(a_1 \omega, SF_2)} \quad (5)$$

where the density ρ is replaced by a function $f(\rho)$ described as $f(\rho) = \rho_v + \left(\frac{\rho_v - \rho_m}{\rho_v - \rho_l}\right)^n (\rho_l - \rho_v)$, a_1 is a constant equal to $5/9$, S represents the strain tensor magnitude ($\bar{S} = \sqrt{2S_{ij}S_{ij}}$) with S_{ij} the components of the strain tensor and the additional functions are calculated as $F_2 = \tanh(\arg_2^2)$, $\arg_2 = \max\left(\frac{2\sqrt{k}}{0.09\omega}, \frac{500v}{y^2\omega}\right)$.

The phase change due to cavitation was included via the Zwart-Gerber-Belamri⁴⁰ model. The model is based on a simplified form of the Rayleigh-Plesset equation⁴¹ and the source terms R_e and R_c corresponding to cavitation bubble expansion and collapse are respectively shown in equations (6) and (7).

$$R_e = F_{vap} \frac{3\alpha_{nuc}(1 - \alpha_v)\rho_v}{R_b} \sqrt{\frac{2p_v - p}{3\rho_l}} \quad \text{if } p < p_v \quad (6)$$

$$R_c = F_{cond} \frac{3\alpha_v\rho_v}{R_b} \sqrt{\frac{2p_v - p}{3\rho_l}} \quad \text{if } p > p_v \quad (7)$$

where F_{vap} and F_{cond} are the evaporation and condensation coefficients. Both are empirical calibration factors with default values of 50 and 0.01, α_{nuc} is the volume fraction associated with the nuclei contained in the liquid taken as 5×10^{-4} and R_b is a representative bubble radius equal to 10^{-6} m.

The thermodynamic properties of the gas phases were derived using NIST REFPROP⁴² to include compressibility effects. The properties of the liquid phase were predicted using the PC-SAFT EoS,⁴³ in which thermodynamic properties can be defined as functions of the residual Helmholtz energy and its derivatives. The transport properties were estimated using the residual entropy scaling method for dynamic viscosity⁴⁴ and thermal conductivity.⁴⁵ In order to reduce the computational cost associated with property calculations using the PC-SAFT EoS, the thermodynamic and transport properties of the fuel were calculated prior to the CFD simulations and stored in structured tables, thereby decoupling the evaluation from the flow calculation and accelerating the simulation.⁴⁶ The temporal and spatial discretization was performed with a second-order and first-order differencing scheme, using an implicit, pressure-based, fully coupled solver.

Computational setup

Taking advantage of the symmetry in the injector design in order to reduce the computational overhead, only one injector hole was included in the computational domain (1/7 sector of the nozzle tip). The computational domain consisted of the inlet, housing wall, needle wall, side surfaces, and discharge volume as shown in Figure 2. The outlet domain or discharge volume was a 1.5 mm long conical volume to reduce the influence of the outlet boundary condition on spray propagation.

The computational domain was discretized using a fully hexahedral mesh to control the number of elements and accelerate the convergence. Furthermore, to better capture small-scale cavitation structures, some strict quality criteria were defined to ensure the cell quality, minimizing discretization and model errors.⁴⁷ The volume-change ratio between neighboring cells was kept below 5, with a minimum cell angle of 22.5° and 3D determinant (normalized triple product of the vectors starting from each cell node) above 0.5 for both key-grids.

The Taylor micro-scales were considered for the cell size definition in the bulk flow region. In this study, the needle position and shape lead to different in-flow velocities. Hence, the Reynolds number based on the spray hole diameter can be estimated to be between 61,000 and

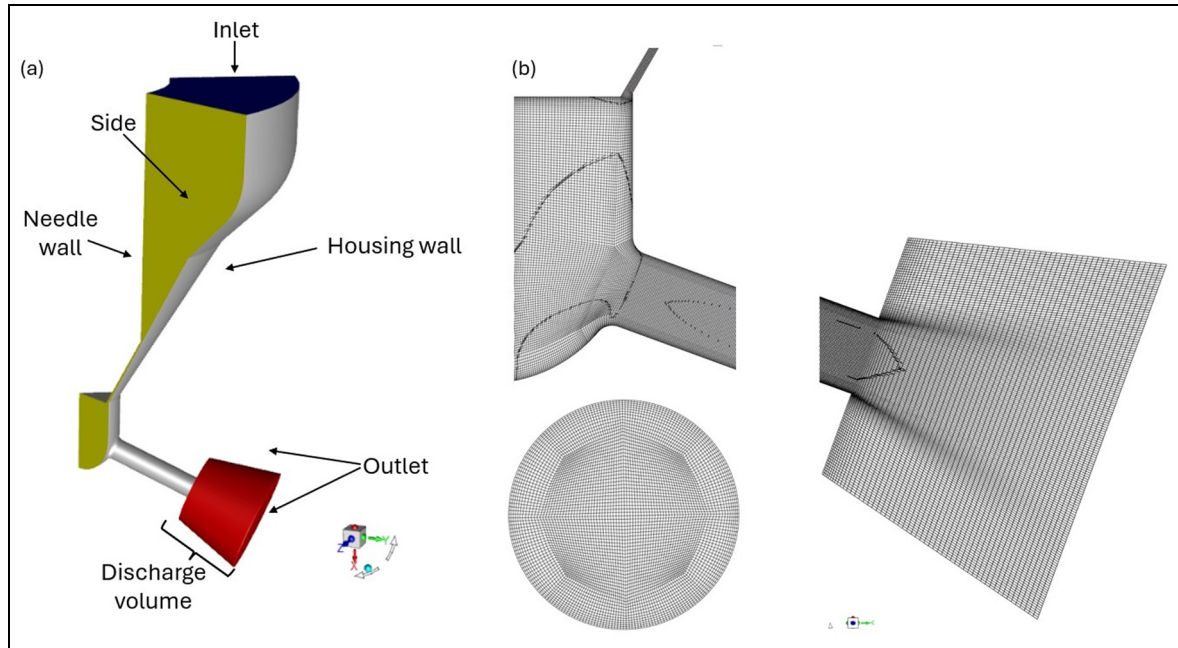


Figure 2. (a) Schematic of the computational domain. (b) Section view of the grid topology in the injector hole and downstream-chamber regions. The final grid corresponds to the base design at low-lift position.

Table 1. Geometry annotation and mesh metrics for the examined designs.

Case	Needle design	Lift (μm)	Cell count	Min. Orth. Quality
1	Base	54	3.29M	0.325
2	NV-01	54	3.41M	0.381
3	NV-02	54	3.28M	0.291
4	NV-03	54	3.15M	0.291
5	Base	480	4.16M	0.251
6	NV-01	480	4.15M	0.250
7	NV-02	480	4.18M	0.285
8	NV-03	480	4.02M	0.248

92,000 for the four geometries at the two lift positions. The Taylor micro-scales can be estimated between 4.1 and 3.3 μm . The maximum mesh resolution was defined based on those criteria and the grid independence study is presented in Appendix 1. The mesh inside the injector spray hole had a maximum cell size of 4.2 μm to avoid an excessive cell count. Further away from the nozzle exit, the mesh becomes coarse with a maximum resolution of 46.3 μm at the outlet region. Under these constraints, the mesh comprises around 4M elements at 480 μm needle lift and 3M at 54 μm . This mesh strategy and final resolution has been verified at full lift for a different injector from Woodward L'Orange and is able to predict the mass flow rate with a difference below 3% in comparison to the experimental measurements.

In addition, for each geometry, the needle was simulated in two positions: high lift at 480 μm and pilot lift at 54 μm . In total, 8 geometries were generated and

Table 1 summarizes the nomenclature used as well as the numerical grid metrics for each one of them.

The boundary conditions were kept constant in all simulations. The in-nozzle region was initialized to contain pure n-dodecane while the chamber downstream of the injector nozzle contained nitrogen. At the inlet, fixed pressure and temperature values of 1600 bar and 343 K were imposed, while the outlet conditions were set to 50 bar and 780 K. A symmetry boundary condition was applied to the side surfaces. Additionally, the nozzle walls were considered adiabatic. Figure 2 depicts the computational domain, boundary conditions and grid topology.

Validation

The implemented numerical methodology was validated via flow rate measurements and X-ray phase contrast radiographies, which highlighted the extent of cavitation in the single-hole Spray C (serial 210037) injector reported in the ECN (Engine Combustion Network) database.⁴⁸ The Spray C nozzle has nominal inlet and outlet diameters of 185 and 208 μm , respectively. The orifice length is 1.0 mm and the injector K-factor is -2.5 . The orifice was drilled off-center with a sharp inlet corner to disturb the flow, thereby inducing cavitation up to the flow separation.

The injector flow was simulated under steady state at a needle lift of 271 μm to match the experimental conditions. The injection pressure was kept constant at 1500 bar as the inlet boundary condition and the ambient pressure was 20 bar, once again, in consistency with

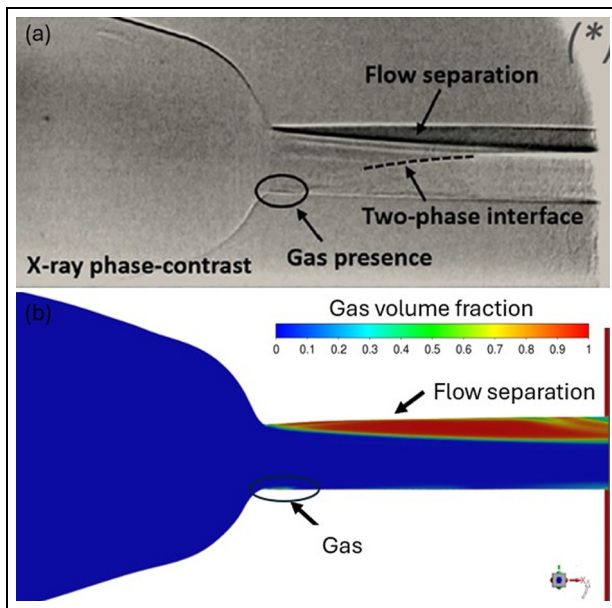


Figure 3. Validation of the numerical methodology against X-ray data for the axial development of the two-phase flow field in the Spray C benchmark injector: (a) X-ray phase contrast radiography, (b) contour plot of gas fraction at the orifice mid-plane.

the X-ray experiments. The working medium, dodecane, was modeled at 343 K, while the ambient temperature was set to 303 K. The presence of non-condensable gas was not included in the model. The computational mesh was a three-dimensional domain with a structured hexahedral topology.

Figure 3 shows a comparison of the line-of-sight radiography (Figure 3(a)) against a contour plot of the gas volume fraction at a plane passing through the orifice axis of symmetry (Figure 3(b)). The X-ray image illustrates a strong flow separation at the upper region of the spray hole, accompanied by the formation of a cavitation sheet attached to the wall. Vapor starts forming at the sharp hole entrance and is convected downstream all the way to the orifice outlet. In addition, a minor gas pocket can be seen at the lower part of the hole entrance. The numerical results are able to reproduce the two-phase flow topology arising in the injector hole.

Furthermore, the numerical data have been compared against X-ray images at six cross-sectional planes along the orifice length, as shown in Figure 4. Overall, the numerical simulation was able to accurately predict the shape of the vapor region along the injector hole periphery, including the thin liquid film observed in the upper part of the plane at $-134 \mu\text{m}$. Some observed differences may be attributed to shot-to-shot variability and temporal fluctuations during the experimental measurement. The X-ray phase contrast image represents a time-averaged measurement and the numerical simulation is a steady-state flow.

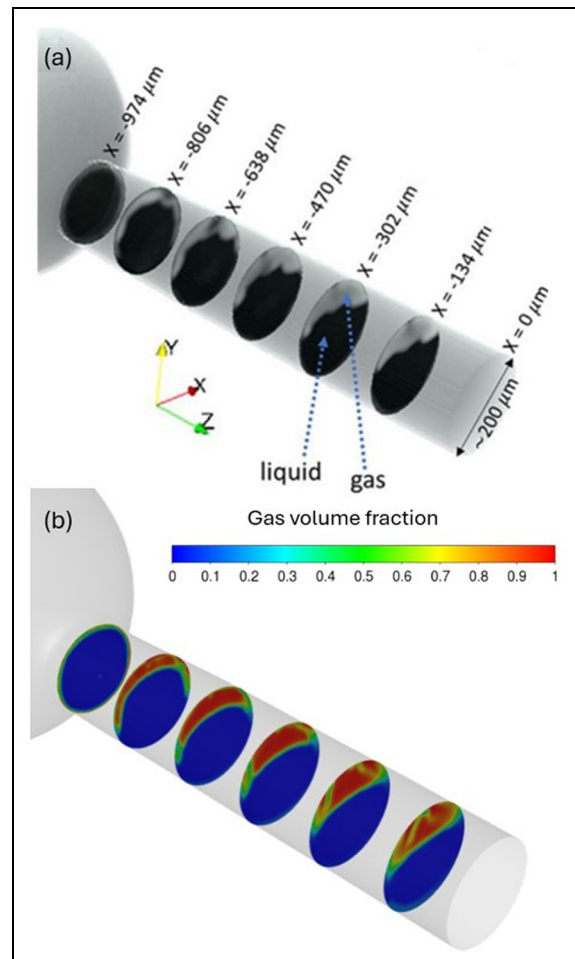


Figure 4. Validation of the numerical methodology against X-ray data for the radial development of the two-phase flow field in the Spray C: (a) X-ray radiographies at different cross-flow planes and (b) Cross-flow contour plots of the vapor field.

Finally, to complement this qualitative validation, Payri et al.⁴⁹ measured the mass flow rate of the Spray C injector under the present operating conditions and reported a value of $(10.07 \pm 0.11) \text{ g/s}$. The respective value predicted by the numerical simulation was 10.47 g/s . In summary, the CFD simulation results show good consistency with the experimental data, reproducing the main flow characteristics as well as the in-nozzle gas distribution.

Results

In order to facilitate the interpretation of the designs, the comparison of the four needle-tip designs was structured into two parts, focusing on the dual-fuel operation (low-needle position or pilot injection) and Diesel-only operation (high-needle position). The parameters analyzed included mass flow, cavitation morphology, velocity, pressure, and three flow coefficients. The mass flow and flow coefficients were determined at the exit of the injector spray hole.

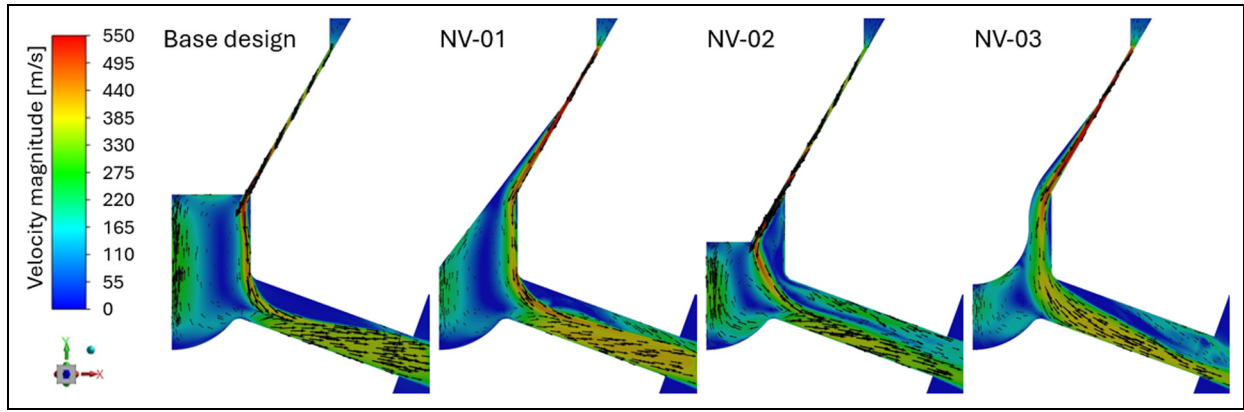


Figure 5. Vector-over-contour plots showcasing the velocity field in the nozzle spray hole mid-plane for the four needle-tip designs examined at pilot injection condition.

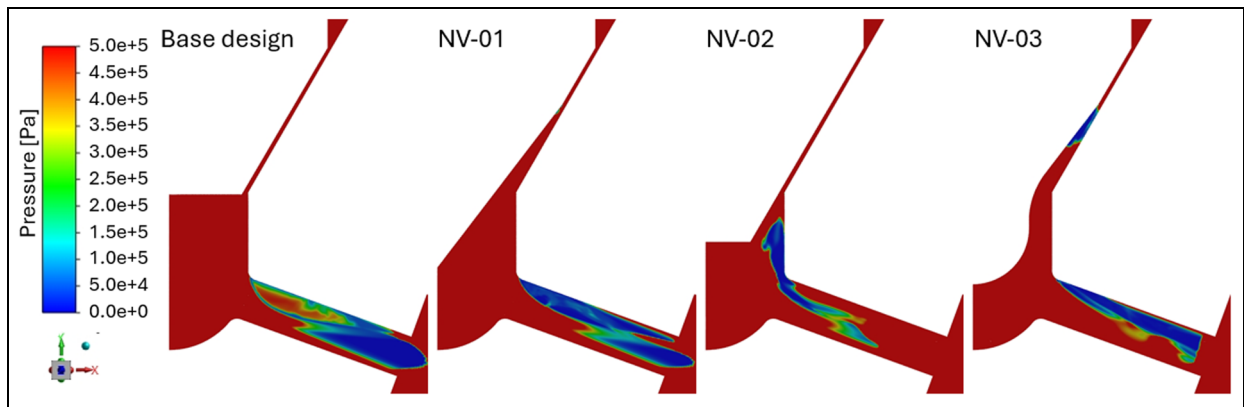


Figure 6. Pressure distribution in the nozzle spray hole mid-plane for the four needle-tip designs examined at pilot injection condition.

In-nozzle flow characteristics during pilot injection (dual-fuel mode)

Figure 5 shows the influence of the needle-tip design on the velocity field at the spray hole mid-plane. The low needle position generates a constricting zone between the needle and the injector seat, which accelerates the flow in this region, causing it to enter the orifice at high velocities along the lower half of the spray hole. This restricted passage has an impact on fluid redirection and varies significantly based on the needle-tip design.

In the base and NV-02 designs, the fluid flows closer to the needle and seat walls. The flow remains attached to the sac wall in the base design until a boundary layer separation from the wall occurs due to the redirection of the high-velocity flow at the spray hole inlet. This separation causes a flow contraction that results in a pressure drop within the spray hole, as depicted in Figure 6. The pressure threshold plotted in the contours is limited to 5 bar in order to emphasize the reduced static pressure regions. Conversely, the needle elongation on NV-02 results in flow separation from the sac's

side wall, as the flow tends to remain attached to the needle wall. The reduced static pressure zone is repositioned within the sac, resulting in a more uniform velocity distribution within the spray hole exit.

In the NV-01 and NV-03 designs, the fluid flows closer to the injector seat wall and is detached from the needle wall due to the deflection angle incorporated in those designs. Despite the deflection angle being minor (below 10°), boundary layer separation can be observed due to the low-pressure zone created at both valve seats in Figure 6. In both designs, the high-velocity flow remains adjacent to the wall in the sac. Nonetheless, the elongation and roundness transitions of the needle in NV-03 lead to a flow deceleration as depicted in Figure 5, reaching the spray hole with lower velocity than NV-01. Additionally, a vena contracta is generated in the spray hole, which further enhances the flow acceleration and reduces the pressure in the upper part of the spray hole.

These low-pressure zones are critical for cavitation onset, occurring when the static pressure drops below the vapor pressure of the continuous fluid.⁵⁰ They

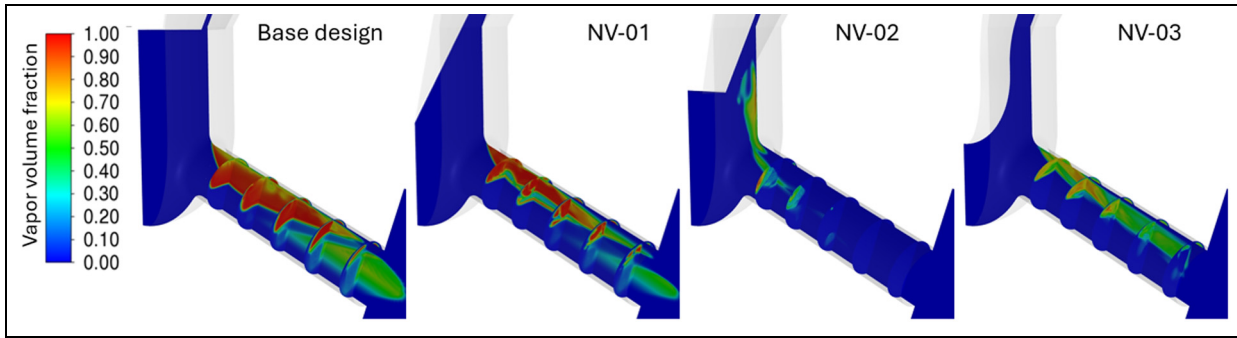


Figure 7. Contour plots of the vapor volume fraction at different axial and cross-flow planes in the injector hole for the four needle-tip designs examined at pilot injection condition.

Table 2. Normalized vapor volume and mass flow rate for different needle-tip designs at pilot injection condition.

Design	Normalized vapor volume (%)	\dot{m}_f (g/s)
Base	13.58	14.30
NV-01	9.60	15.96
NV-02	5.77	13.03
NV-03	5.98	14.03

Table 3. Dimensionless flow coefficients for different needle-tip designs at pilot injection condition.

Design	C_d	C_v	C_a
Base	0.396	0.478	0.828
NV-01	0.443	0.520	0.853
NV-02	0.363	0.363	0.999
NV-03	0.387	0.391	0.989

increase the hydraulic resistance and may cause violent collapse of cavitation structures, generating high-pressure peaks that can erode injector surfaces.²⁴ At the same time, the cavitation structures can enhance fuel atomization and spray formation.^{14,51} Therefore, a balanced approach is essential to harness the benefits of cavitation while mitigating its adverse effects.

The phase transition from the liquid to vapor is illustrated in Figure 7. The contour plots of the vapor volume fraction are presented at the orifice plane of symmetry and five equidistant cross-flow planes. Cavitation can be closely associated with the low-pressure zones depicted in Figure 6. Furthermore, no significant vapor was observed in the lower pressure zone of the valve seat for NV-01 and NV-03 designs. Consequently, the contour plots focus exclusively on the sac and spray orifices.

As expected, the base, NV-01 and NV-03 designs exhibit cavitation at the spray hole inlet, with vapor formation along the upper surface of the spray hole. NV-02 is the only design in which cavitation is mitigated within the spray hole by relocating it into the sac volume. Cavitation in the sac volume can disrupt the internal flow, resulting in irregular fuel delivery and reduced mass flow rates.^{52,53} This location presents considerable risks in comparison to cavitation occurring in the spray hole. In contrast, regulated cavitation in the spray hole can enhance atomization and improve combustion efficiency.³² Qualitatively, all proposed designs reduced the cavitation intensity and the vapor content within the nozzle as detailed in Table 2. To facilitate the

comparison of the designs, the vapor volumes were normalized by the total of the sac and spray hole volumes.

The base design induces a higher amount of vapor, followed by NV-01, whereas designs NV-02 and NV-03 exhibit comparable vapor volumes. Nonetheless, cavitation intensity and mass flow rate do not follow a linear relationship. The magnitude and location of cavitation are crucial. The vapor bubbles reduce the flow area and can increase the flow resistance, typically resulting in a reduction of the mass flow rate.⁴⁹ In some cases, properly controlled cavitation can increase the mass flow and consequently the discharge coefficient of the injector, thereby enhancing fuel flow rate and improving overall efficiency of the injection process.⁵⁴ The onset of cavitation and its impact on mass flow rate are also affected by the fuel saturation pressure and heating value.¹⁶ Because the four designs are under the same operation conditions and were computed with the same fuel, the geometry is primarily responsible for the correlation between cavitation and mass flow rate in this study.

In complement, Table 3 shows the injector flow behavior in terms of flow coefficients. The discharge coefficient C_d , described as $C_d = \left(\frac{\dot{m}_f}{A_o \sqrt{2\rho_f \Delta P}} \right)$, represents the ratio between the theoretical mass flow and the actual mass flow, indicating the injector's capability to deliver the required fuel quantity.

Since the pressure difference (ΔP) between inlet and ambient pressure remains constant among all cases, the C_d is mainly a consequence of the mass flow rate (\dot{m}_f) and the liquid density (ρ_f). Cavitation in the region

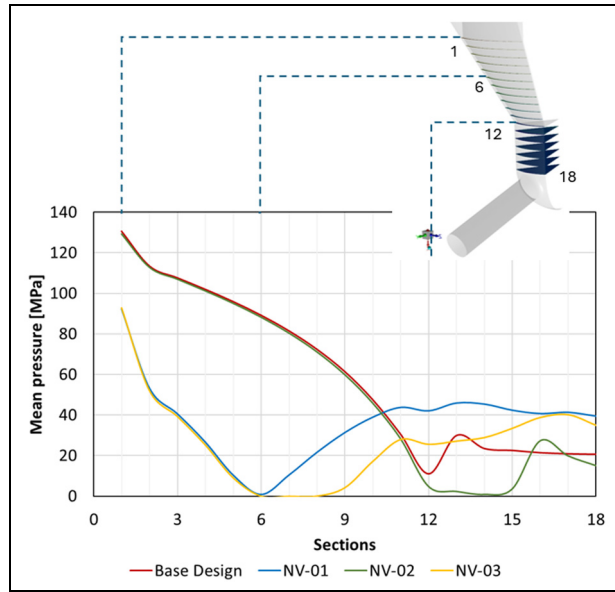


Figure 8. Average pressure distribution along the needle seat and sac volume for the four needle-tip designs at pilot injection condition.

upstream of the spray hole induces flow acceleration, resulting in an increase of the discharge coefficient of NV-01 design in comparison to the base design. For the NV-02 and NV-03 designs, the discharge coefficient is slightly reduced, despite exhibiting a decreased vapor volume. The C_d can also be described in terms of the velocity coefficient C_v and the area coefficient C_a , as they are related by the equation $C_d = C_v C_a$.

The velocity coefficient $C_v = \left(\frac{u_{eff}}{u_{th}} \right)$ represents the ratio of the actual flow velocity to the theoretical velocity, signifying the kinetic energy of the fuel jet as it exits the nozzle. The same positive impact of NV-01's flow acceleration can be seen in terms of the velocity coefficient (C_v) and a reduction of this value for the other designs in comparison to the base design.

The third non-dimensional flow parameter is the area coefficient $C_a = \left(\frac{A_{eff}}{A_o} \right)$, which correlates the effective flow area to the geometric orifice area and considers the contraction of the flow streamlines as the fuel passes through the orifice. This metric also takes into account the flow separation areas. The base design, followed by NV-01, has the lowest effective area, which correlates with the normalized vapor volume in the injector hole in those designs.

Finally, a smooth and higher-pressure build-up inside the sac volume is a relevant characteristic that may contribute to a stable and consistent injection.⁵² Elevated sac pressures create a better outward momentum that aids in preventing the ingress of external gases into the nozzle holes.⁵⁵ However, injector components may be susceptible to wear and tear as consequence of excessive high pressure, thereby potentially reducing their lifespan and increasing maintenance costs.⁵⁶

The progression of the average pressure in the needle seat and sac volume is quantified in Figure 8, illustrating the pressure variation exerted on the fluid before reaching the spray hole. The planes 1–12 denote the average pressure in the seat region, where the deflection angle from NV-01 and NV-03 designs is located between planes 7 and 8. The sac region is covered from plane 12 to 18 and shortly before the spray hole inlet.

The base and NV-02 designs exhibited the highest pressure up to the 10th probing plane with intensity progressively diminishing toward the needle-tip. After the 12th section, the base design facilitates pressure recovery within the sac volume. The pressure recovery in NV-02 design occurs only after the end of the needle-tip elongation and was further delayed due to flow separation and the low-pressure areas in the sac volume. Despite those impacts, the base and NV-02 designs maintain the same pressure close to the spray hole inlet. The deflection angle on NV-01 and NV-03 designs results in a pressure drop along the needle seat compared to the previous designs. Subsequent to the sixth section, the pressure began to recover, resulting in an elevated pressure within the sac volume, which is nearly double that of the base design in the spray hole inlet area.

In-nozzle flow characteristics at high needle lift (Diesel-only mode)

The impact of the needle-tip design on the velocity field is shown in Figure 9 at the spray hole mid-plane. Unlike the low needle position, the region between the needle and injector seat forms a larger flow passage, resulting in reduced constriction. This passage accelerates the flow, directing it through the sac volume and into the spray hole with elevated velocities compared to the low needle lift cases. However, the redirection of an accelerated flow is less abrupt and as a consequence a boundary layer separation is not created from the wall in the seat and sac walls.

In all designs, the spray hole inlet acts as the primary flow constraint, imposing an abrupt deflection that causes flow detachment from the upper wall inside the spray hole. The separated boundary layer forces the main flow to redirect, creating a turbulent, low-pressure region behind the separation point. These separation points can be verified via the adverse pressure gradients shown in Figure 10. Similar to the low lift investigation, the pressure distribution was also limited to 5 bar.

This adverse pressure gradient further retards the already slow-moving boundary layer. The flow streamlines converge downstream of the separation point, creating a vena contracta in all four simulated geometries. Nonetheless, the influence of the additional flow acceleration and the formed low pressure region is manifesting with different intensities. All proposed designs qualitatively result in an expansion of the vena contracta relative to the base design, which expands

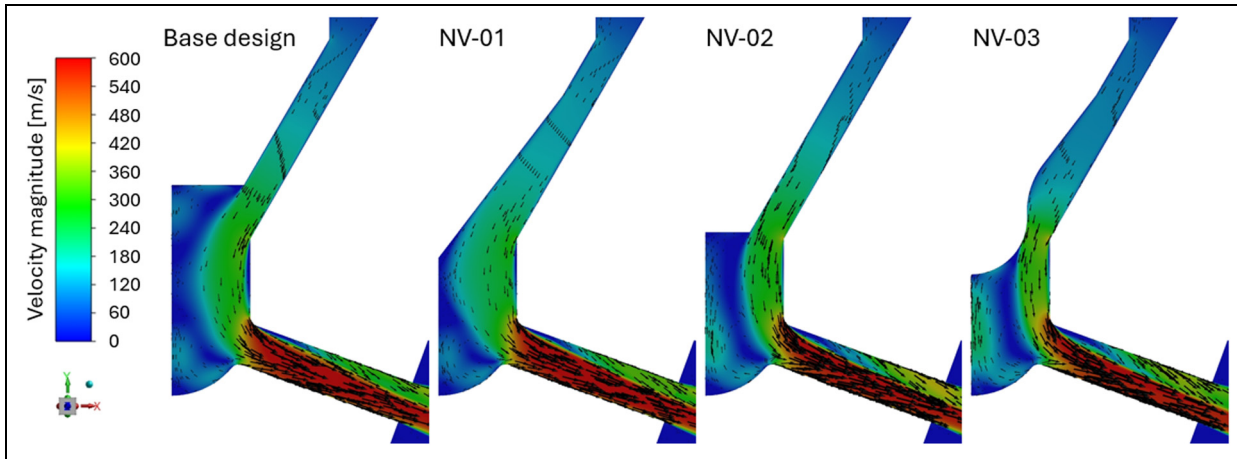


Figure 9. Vector-over-contour plots showcasing the velocity field in the nozzle spray hole mid-plane for the four needle-tip designs examined at Diesel-only injection condition.

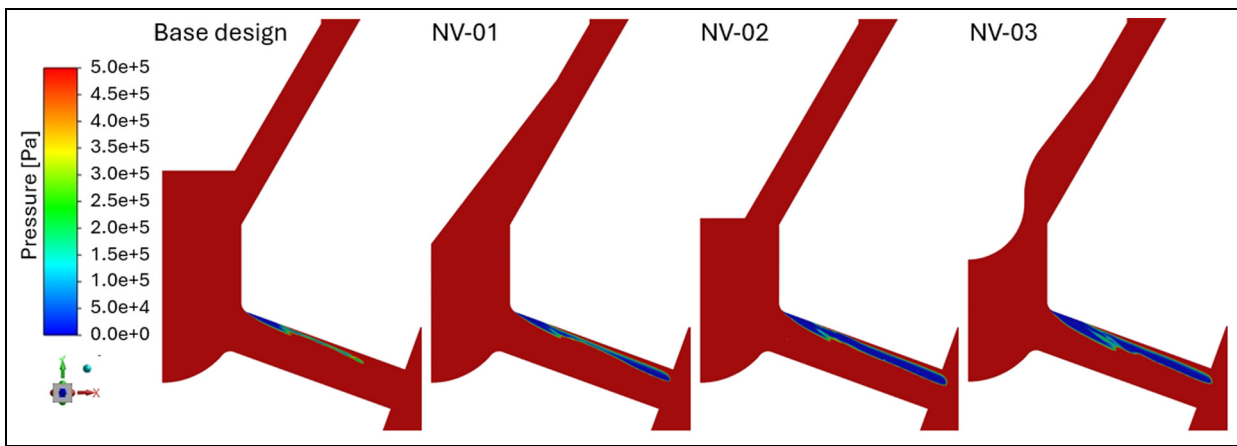


Figure 10. Pressure distribution in the nozzle spray hole mid-plane for the four needle-tip designs examined at Diesel-only injection condition.

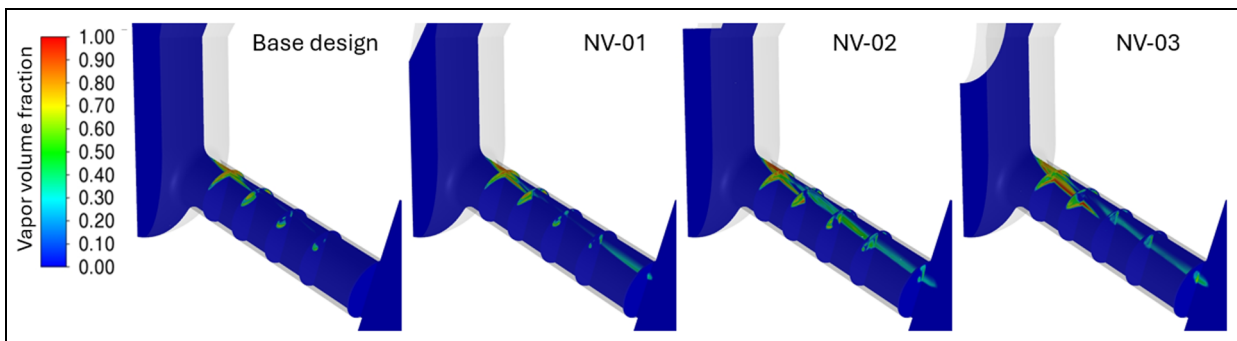


Figure 11. Contour plots of the vapor volume fraction at different axial and cross-flow planes in the injector hole for the four needle-tip designs examined at Diesel-only injection condition.

toward the spray hole exit. The larger vena contracta accelerates the flow in the lower part of the spray hole, intensifying the pressure decrease and enhancing the cavitation phenomena.

The vapor volume fraction is shown in Figure 11 for all four designs simulated. In all cases, cavitation occurs at the upper region of the hole entrance within the low-pressure zones. The base design exhibits a

Table 4. Normalized vapor volume and mass flow rate for different needle-tip designs at Diesel-only injection condition.

Design	Normalized vapor volume (%)	\dot{m}_f (g/s)
Base	1.59	31.08
NV-01	1.61	31.13
NV-02	2.07	28.82
NV-03	2.17	27.35

lower amount of vapor compared to the other design modifications. Subsequently, NV-01 exhibits a more dispersed vapor cloud along the spray hole. NV-02 and NV-03 designs demonstrate an increased vapor volume at the spray hole.

The volume vapor volume is quantified in Table 4. This value was normalized by the sum of the sac and orifice volumes. As anticipated from the qualitative images analyses, the base design presents the lowest volume of vapor and the NV-01 does not present a meaningful difference to the base design. An similar conclusion can be drawn for NV-02 and NV-03 designs as the normalized vapor volume are equivalent between those designs.

Similar to Tables 3 and 5 presents the flow behavior in terms of flow coefficients. At a high lift, the influence of the needle on flow rate is less pronounced than during pilot injection.

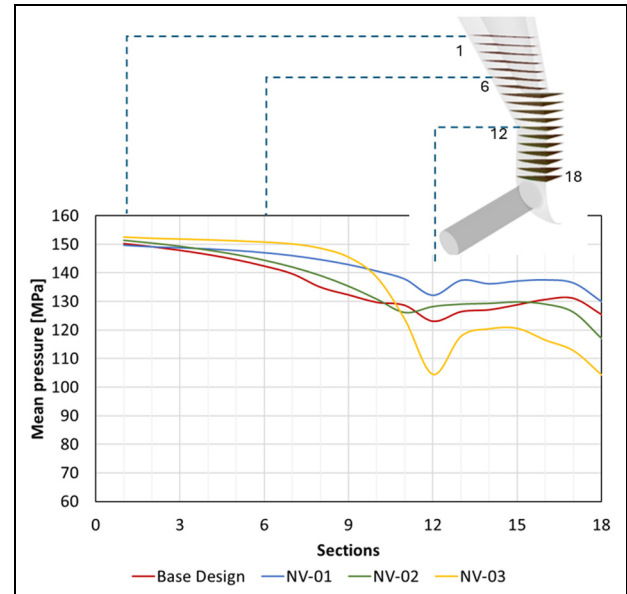
The analogous behavior of base and NV-01 designs is reflected in the C_d and C_v , which exhibit comparable orders of magnitude. The relocation of flow separation inside the spray hole lowers the performance in terms of C_d and C_v for NV-02 in comparison to the base design. The curved needle surface of NV-03 design also induces a reduction of both coefficients but performs slightly better than the NV-02 one.

Furthermore, the reduction in effective liquid-phase area is negligible across all designs as indicated by C_a . In the high lift position, cavitation at the exit of the spray hole is minimal and neither flow separation nor hydraulic flip is observed at the spray hole exit in these designs. Consequently, the effective area of the liquid phase approaches values near 1.

Finally, the pressure in the needle seat and sac volume can be quantified prior to the fluid reaching the spray hole, as shown in Figure 12. The NV-01 design enhances pressure maintenance in the needle seat and sac volume from the first to the ninth segment, outperforming the base design. The NV-02 design exhibits comparable performance to base design for the average pressure. Both designs restrict the pressure drop in the sac volume to approximately 300 bar lower relative to the rail pressure. The NV-03 design presents the highest pressure in the needle seat area, from the first to the ninth section. After the ninth section, the pressure drops considerably, reaching its lowest value in the sac volume.

Table 5. Dimensionless flow coefficients for different needle-tip designs at Diesel-only injection condition.

Design	C_d	C_v	C_a
Base	0.832	0.835	0.996
NV-01	0.833	0.837	0.995
NV-02	0.739	0.741	0.997
NV-03	0.777	0.781	0.995

**Figure 12.** Average pressure distribution along the needle seat and sac volume for the four needle-tip designs at Diesel-only injection condition.

Conclusion

This paper presented numerical simulations revealing the impact of needle-tip design on internal nozzle flow and cavitation in marine Diesel injectors. The numerical model has been enhanced by incorporating NIST and PC-SAFT EoS calculations through a tabulated thermodynamic method. The inclusion of NIST and PC-SAFT EoS provides a good prediction as evaluated against experimental data regarding mass flow and cavitation regions under typical operating conditions of Diesel engines. In order to enhance the base design geometrical features that lead to under-performance during dual-fuel operating conditions, and to ensure fuel flexibility across the complete engine operation range, three needle-tip designs were proposed.

The redesign of the needle-tip was selected for its simplicity and cost-effectiveness compared with nozzle design modifications. The base design was evaluated against three proposed alternatives to assess performance in two operational modes: Diesel-only and dual-fuel. At low needle lifts (dual-fuel mode), the three proposed needle-tip designs reduced vapor formation

within the injector, but NV-02 shifted the vapor-generation region into the sac rather than the spray hole in contrast to the other designs. In addition, NV-01 and NV-03 designs promoted a better pressure recovery in the sac volume, a crucial factor for pilot injection conditions.

In high needle lifts (Diesel-only mode), the base and NV-01 designs exhibited comparable performance regarding cavitation location, fuel delivery and flow coefficients. NV-02 and NV-03 designs slightly increased the amount of vapor generated inside the spray hole, also reducing the performance as indicated by the flow coefficients. NV-01 is the only design that increases the sac pressure compared to the base design. Finally, focusing on the fuel flexibility for marine applications, the NV-01 design enhances pilot injection operation without compromising the high lift performance, offering the best trade-off in terms of flow assessment for both operational modes.


Funding

The authors disclosed receipt of the following financial support for the research, authorship, and/or publication of this article: This work has received funding from the European Union's Horizon 2020 research and innovation program under the Marie Skłodowska-Curie grant agreement No 861002.

Declaration of conflicting interests

The authors declared no potential conflicts of interest with respect to the research, authorship, and/or publication of this article.

ORCID iD

Marilia G. Justino Vaz  <https://orcid.org/0000-0002-2367-0360>

References

1. EU. Commission regulation (EU) no 582/2011 of 25 may 2011 implementing and amending regulation (EC) no 595/2009 of the European parliament and of the council with respect to emissions from heavy duty vehicles (Euro VI) and amending annexes I and III to direct. *Off J European Union* 2011.
2. Bick W, Köhne M, Pape U, et al. The new deutz tier 4 engines. *MTZ Worldw* 2010; 71(10): 4–10.
3. Çabukoglu E, Georges G, Küng L, et al. Battery electric propulsion: an option for heavy-duty vehicles? Results from a Swiss case-study. *Transp Res Part C: Emerg Technol* 2018; 88: 107–123.
4. Stoumpos S, Theotokatos G, Mavrelos C, et al. Towards marine dual fuel engines digital twins—integrated modelling of thermodynamic processes and control system functions. *J Mar Sci Eng* 2020; 8(3): 200.
5. Wärtsilä. *Wärtsilä 34DF Product Guide*. Wärtsilä, 2020.
6. Watanabe K. High operation capable marine dual fuel engine with lng. *J Jpn Inst Mar Eng* 2015; 50(6): 738–743.
7. Wärtsilä. *Lng shipping solutions*. Wärtsilä, 2017.
8. Redtenbacher C, Kiesling C, Wimmer A, et al. Dual fuel brennverfahren - ein zukunftsweisendes konzept vom pkw- bis zum großmotorenbereich? In: H Lenz (ed.) *Tagungsband, 37. Internationales Wiener Motorensymposium*. VDI Verlag Wien, 2016, pp. 403–428, Vol. 799.
9. Xia J, Zhang Q, Wang J, et al. Experimental study on the combustion and soot emission of twin-spray collision at various collision angles and injection pressures under marine engine's conditions. *Int J Engine Res* 2023; 24(8): 3783–3794.
10. Coppo M, Pinkert F, Negri C, et al. Detailed characterisation and service experience of OMT injectors for dual-fuel medium- and low-speed engines. In: *29th CIMAC World Congress*, Vancouver, Canada, 2019.
11. Karathanassis IK, Heidari-Koochi M, Koukouvini F, et al. Quantification of cavitating flows with neutron imaging. *Sci Rep* 2024; 14: 26911.
12. Moon S, Huang W, Li Z, et al. End-of-injection fuel dribble of multi-hole diesel injector: Comprehensive investigation of phenomenon and discussion on control strategy. *Appl Energy* 2016; 179: 7–16.
13. Moon S, Huang W and Wang J. First observation and characterization of vortex flow in steel micronozzles for high-pressure diesel injection. *Exp Therm Fluid Sci* 2019; 105: 342–348.
14. Andriotis A, Gavaises M and Arcoumanis C. Vortex flow and cavitation in diesel injector nozzles. *J Fluid Mech* 2008; 610: 195–215.
15. Battistoni M, Som S and Longman DE. Comparison of mixture and multifluid models for in-nozzle cavitation prediction. *J Eng Gas Turbine Power* 2014; 136(6): 061506.
16. Torelli R, Som S, Pei Y, et al. Influence of fuel properties on internal nozzle flow development in a multi-hole diesel injector. *Fuel* 2017; 204: 171–184.
17. Theodorakakos A, Strotos G, Mitroglou N, et al. Friction-induced heating in nozzle hole micro-channels under extreme fuel pressurisation. *Fuel* 2014; 123: 143–150.
18. Yu Y. Experimental study on effects of ethanol-diesel fuel blended on spray characteristics under ultra-high injection pressure up to 350 MPa. *Energy* 2019; 186: 115768.
19. Vidal A, Kolovos K, Gold MR, et al. Preferential cavitation and friction-induced heating of multi-component diesel fuel surrogates up to 450mpa. *Int J Heat Mass Transf* 2021; 166: 120744.
20. Cao T, He Z and Wang J. Investigation of cavitation phenomenon with different fuel temperatures in diesel nozzles. *Adv Mech Eng* 2023; 15(10). DOI: 10.1177/16878132231202867
21. Mitroglou N, McLorn M, Gavaises M, et al. Instantaneous and ensemble average cavitation structures in diesel micro-channel flow orifices. *Fuel* 2014; 116: 736–742.
22. Payri F, Bermúdez V, Payri R, et al. The influence of cavitation on the internal flow and the spray characteristics in diesel injection nozzles. *Fuel* 2004; 83(4-5): 419–431.
23. Payri F, Payri R, Salvador FJ, et al. A contribution to the understanding of cavitation effects in diesel injector

- nozzles through a combined experimental and computational investigation. *Comput Fluids* 2012; 58: 88–101.
24. Koukouvinis P, Gavaises M, Li J, et al. Large eddy simulation of diesel injector including cavitation effects and correlation to erosion damage. *Fuel* 2016; 175: 26–39.
 25. Chouak M, Dufresne L and Seers P. Large eddy simulation of a double-injection cycle and the impact of the needle motion on the sac-volume flow characteristics of a single-orifice diesel injector. *Int J Engine Res* 2021; 22(8): 2464–2476.
 26. Mitroglou N and Gavaises M. Mapping of cavitating flow regimes in injectors for medium-/heavy-duty diesel engines. *Int J Engine Res* 2013; 14(6): 590–605.
 27. Koci CP, Fitzgerald RP, Ikonomou V, et al. The effects of fuel–air mixing and injector dribble on diesel unburned hydrocarbon emissions. *Int J Engine Res* 2019; 20(1): 105–127.
 28. Gavaises M, Murali-Girija M, Rodriguez C, et al. Numerical simulation of fuel dribbling and nozzle wall wetting. *Int J Engine Res* 2022; 23(1): 132–149.
 29. Salvador FJ, Carreres M, Jaramillo D, et al. Comparison of microsac and vco diesel injector nozzles in terms of internal nozzle flow characteristics. *Energy Convers Manag* 2015; 103: 284–299.
 30. Watanabe H, Nishikori M, Hayashi T, et al. Visualization analysis of relationship between vortex flow and cavitation behavior in diesel nozzle. *Int J Engine Res* 2015; 16: 5–12.
 31. Markov V, Sa B, Kamaltdinov V, et al. Investigation on the effect of the flow passage geometry of diesel injector nozzle on injection process parameters and engine performances. *Energy Sci Eng* 2022; 10: 552–577.
 32. He Z, Guo G, Tao X, et al. Study of the effect of nozzle hole shape on internal flow and spray characteristics. *Int Commun Heat Mass Transf* 2016; 71: 1–8.
 33. Som S, Ramirez AI, Longman DE, et al. Effect of nozzle orifice geometry on spray, combustion, and emission characteristics under diesel engine conditions. *Fuel* 2011; 90(3): 1267–1276.
 34. Chen Z, He Z, Shang W, et al. Experimental study on the effect of nozzle geometry on string cavitation in real-size optical diesel nozzles and spray characteristics. *Fuel* 2018; 232: 562–571.
 35. Salvador FJ, Carreres M, Jaramillo D, et al. Analysis of the combined effect of hydrogrinding process and inclination angle on hydraulic performance of diesel injection nozzles. *Energy Convers Manag* 2015; 105: 1352–1365.
 36. Zhang W, Li X, Huang L, et al. Experimental study on spray and evaporation characteristics of diesel-fueled marine engine conditions based on optical diagnostic technology. *Fuel* 2019; 246: 454–465.
 37. A Prosperetti and G Tryggvason. (eds.) *Computational Methods for multiphase flow*. Cambridge University Press, 2007.
 38. Edelbauer W, Struel J and Morozov A. *Large eddy simulation of cavitating throttle flow*. Springer, 2016. pp. 34.
 39. Reboud JL, Stutz B and Coutier O. Two-phase flow structure of cavitation: experiment and modelling of unsteady effects. In: *Third international symposium on cavitation*, Grenoble, France, 1998. DOI: 10.1063/1.869505.
 40. Zwart P, Gerber A and Belamri T. A two-phase flow model for predicting cavitation dynamics. In: *Fifth international conference on multiphase flow*, 2004.
 41. Brennen CE. *Cavitation and bubble dynamics*. Cambridge University Press, 2013.
 42. Lemmon E, Huber M and McLinden M. Nist standard reference database 23: Reference fluid thermodynamic and transport properties-refprop, version 9.1, 2013. https://tsapps.nist.gov/publication/get_pdf.cfm?pub_id=912382
 43. Gross J and Sadowski G. Perturbed-chain saft: an equation of state based on a perturbation theory for chain molecules. *Ind Eng Chem Res* 2001; 40(4): 1244–1260.
 44. Lötgering-Lin O and Gross J. Group contribution method for viscosities based on entropy scaling using the perturbed-chain polar statistical associating fluid theory. *Ind Eng Chem Res* 2015; 54(32): 7942–7952.
 45. Hopp M and Gross J. Thermal conductivity from entropy scaling: a group-contribution method. *Ind Eng Chem Res* 2019; 58(44): 20441–20449.
 46. Rubino A, Pini M, Kosec M, et al. A look-up table method based on unstructured grids and its application to non-ideal compressible fluid dynamic simulations. *J Comput Sci* 2018; 28: 70–77.
 47. Moukalled F, Mangani L and Darwish M. *The finite volume method in computational fluid dynamics: an advanced introduction with OpenFOAM® and Matlab®*. Springer Cham, 2015. Vol. 113.
 48. ECN. Diesel data search page, 2021. <https://ecn.sandia.gov/ecn-data-search/>.
 49. Payri R, Gimeno J, Cuisano J, et al. Hydraulic characterization of diesel engine single-hole injectors. *Fuel* 2016; 180: 357–366.
 50. Som S, Longman D, Ramirez A, et al. Influence of nozzle orifice geometry and fuel properties on flow and cavitation characteristics of a diesel injector. *Fuel Inject Automot Eng* 2012; 111–126. DOI: 10.5772/38900.
 51. Balz R, Nagy IG, Weisser G, et al. Experimental and numerical investigation of cavitation in marine diesel injectors. *Int J Heat Mass Transf* 2021; 169: 120933.
 52. Manin J, Pickett LM and Yasutomi K. Stereoscopic high-speed microscopy to understand transient internal flow processes in high-pressure nozzles. *Exp Therm Fluid Sci* 2020; 114: 110027.
 53. He Z, Zhou H, Duan L, et al. Effects of nozzle geometries and needle lift on steadier string cavitation and larger spray angle in common rail diesel injector. *Int J Engine Res* 2021; 22(8): 2673–2688.
 54. Hassanzadeh A, Saadat Bakhsh M and Dadvand A. Numerical study of the effect of wall injection on the cavitation phenomenon in diesel injector. *Eng Appl Comput Fluid Mech* 2014; 8: 562–573.
 55. Gomez Santos E, Shi J, Gavaises M, et al. Investigation of cavitation and air entrainment during pilot injection in real-size multi-hole diesel nozzles. *Fuel* 2020; 263: 116746.
 56. Makri K, Lockett R and Jeshani M. Dynamics of post-injection fuel flow in mini-sac diesel injectors part 1: Admission of external gases and implications for deposit formation. *Int J Engine Res* 2021; 22(4): 1133–1153.

Appendix I

Grid independence study

The mesh sensitivity study was carried out for a 1/7 sector of the base design at an injection pressure of 1600 bar and an outlet pressure of 50 bar. The effect of the mesh resolution and the impact on the velocity at the spray hole exit are presented in Table 6. A slight variation can be observed between Grid 3 and Grid 4, demonstrating a reasonable achievement of grid convergence. Based on these results, the Grid 3 with a maximum mesh resolution of $4.2\ \mu\text{m}$ inside the injector spray hole was selected in this

Table 6. Velocity sensitivity at the exit of the spray hole for the different grid resolutions.

Grid	Lift (μm)	Cell count	Min. Orth. quality	Velocity (m/s)
1	480	1.42M	0.366	551.59
2	480	2.98M	0.256	554.25
3	480	4.16M	0.251	556.51
4	480	5.76M	0.248	557.38

study, where the other geometries presented an equivalent mesh resolution and quality.